Revealing the kinematic puzzle of the AGN host NGC 3884: optical integral field spectroscopy unravels stellar and gas motions

Rogemar A. Riffel [1]★ Rogério Riffel [2,3] Thaisa Storchi-Bergmann,[2] José Henrique Costa-Souza,[1] Gabriel Luan Souza-Oliveira[1] and Marina Bianchin [3]†

[1]*Departamento de Física, CCNE, Universidade Federal de Santa Maria, 97105-900 Santa Maria, RS, Brazil*
[2]*Departamento de Astronomia, Instituto de Física, Universidade Federal do Rio Grande do Sul, CP 15051, 91501-970 Porto Alegre, RS, Brazil*
[3]*Instituto de Astrofísica de Canarias, Calle Vía Láctea s/n, E-38205 La Laguna, Tenerife, Spain*

ABSTRACT

We used optical integral field spectroscopy to analyse the stellar and gas properties of the inner 1.4 kpc radius of NGC 3884, a low-luminosity active galactic nucleus (AGN) host. The observations were performed with Gemini Multi-Object Spectrograph (GMOS)-Integral Field Unit at a seeing of ∼0.85 arcsec (475 pc at the galaxy) that allowed us to map the stellar and gas emission structure and kinematics, for the first time in this galaxy. The stellar motions are consistent with rotation in a disc, with the kinematic position angle (PA) ranging from approximately 0° within 500 pc to 20° beyond 1 kpc, consistent with the photometric PA. We detected extended ionized and neutral gas emission throughout most of the GMOS field of view, with three kinematic components: (i) a disc component with a kinematic PA similar to that of the stars beyond ∼670 pc from the nucleus; (ii) a twist in the PA of up to 60° at a smaller radii that we attribute to gas inflow towards the nucleus; and (iii) an outflow detected as broad components to the emission lines ($\sigma \sim$ 250–400 km s^{-1}), with a maximum mass outflow rate of 0.25 ± 0.15 M$_\odot$ yr^{-1} and a kinetic power corresponding to 0.06 per cent of the AGN bolometric luminosity, possibly being powerful enough to suppress star formation in the galaxy. The observed gas kinematics thus reveals both inflows and outflows in ionized gas.

Key words: galaxies: active – galaxies: individual: NGC 3884 – galaxies: kinematics and dynamics.

1 INTRODUCTION

In the last few decades, observational studies have provided strong support for the co-evolution of galaxies and supermassive black holes (SMBHs; Magorrian et al. 1998; Ferrarese & Merritt 2000; Gebhardt et al. 2000; Caglar et al. 2020). This co-evolution is attributed to the processes of feeding (e.g. Storchi-Bergmann & Schnorr-Müller 2019) and feedback of active galactic nuclei (AGNs). Feedback mechanisms involve the emission of jets from the inner boundary of the accretion disc, winds from the outer regions of the disc, and radiation from the hot gas in the disc or its corona (e.g. Elvis 2000; Frank, King & Raine 2002). Scaling relations between the mass of SMBHs and their properties can be established by harnessing a small portion of the luminosity emitted by powerful AGN to drive a wind, as indicated by analytical models (e.g. Silk & Rees 1998; King 2003). However, the role of AGN feedback in determining these scaling relations remains a topic of debate (Peng 2007; Graham & Sahu 2023).

Currently, it is widely recognized that AGN feedback processes play a crucial role in shaping galaxies, by heating the gas within and surrounding them, and consequently suppressing star formation during cycles of nuclear activity (Binney & Tabor 1995; Silk &

Rees 1998; Di Matteo, Springel & Hernquist 2005; Hopkins & Elvis 2010; Schaye et al. 2015; Silk 2017; Weinberger et al. 2017; Costa et al. 2018; Harrison et al. 2018). In addition, multiphase AGN winds can expel or redistribute gas, preventing its collapse into stars. Determining the properties of the outflows in multiple gas phases is fundamental to properly understand their role in the evolution of galaxies, providing observational constraints to cosmological simulations (Feruglio et al. 2010, 2015; Liu et al. 2013; Cicone et al. 2014; Ramos Almeida et al. 2017; Rupke et al. 2019; Shimizu et al. 2019; Couto et al. 2020; Kakkad et al. 2020, 2022; Comerón et al. 2021; Dall'Agnol de Oliveira et al. 2021, 2023; Riffel et al. 2021c; Ruschel-Dutra et al. 2021; Heckler, Ricci & Riffel 2022; Juneau et al. 2022).

In this work, we use optical integral field spectroscopy (IFS) to spatially resolve the emission structure and kinematics of the neutral and ionized gas in the central region of NGC 3884. This galaxy was selected as a likely host of powerful molecular gas outflows, based on the sample presented in Riffel, Zakamska & Riffel (2020), using mid-infrared and optical observations. These authors selected their sample by cross-matching a parent sample of 2015 galaxies ($0.002 \leq z \leq 3.0$) with *Spitzer* mid-infrared spectra from Lambrides et al. (2019) and the Sloan Digital Sky Survey (SDSS) spectroscopic data base (Gunn et al. 2006; Blanton et al. 2017). This resulted 309 galaxies with both SDSS and *Spitzer* spectra available, and 115 of them with the H$_2$ S(3) 9.665 μm and polycyclic aromatic hydrocarbon (PAH) 11.3 μm

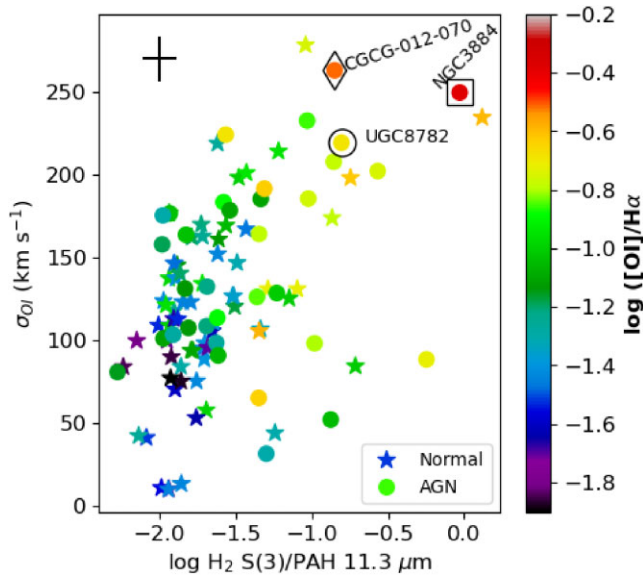★ E-mail: rogemar@ufsm.br
† IAU-Gruber Foundation Fellow.

Figure 1. Updated version of fig. 1 of Riffel et al. (2023), showing the plot of the [O I] velocity dispersion versus the H_2 S(3)/PAH 11.3 μm ratio for the sample of Riffel, Zakamska & Riffel (2020). The colour of the points corresponds to their [O I] λ6300/Hα values, which are indicated by the scale bar. BPT-selected AGN hosts are denoted by filled circles, while normal galaxies are represented by stars. The top-left corner shows the typical uncertainties. NGC 3884 is identified by the open square and UGC 8782, discussed in Riffel et al. (2023), is shown as an open circle. CGCG 012−070 is identified by a diamond. Objects located at the top-right corner are interpreted as the most likely hosts of strong outflows in molecular gas by Riffel, Zakamska & Riffel (2020).

emission lines detected. The mid-infrared observations from the *Spitzer Space Telescope* reveal that AGN hosts present a significant excess of H_2 emission when compared to the expected emission from normal star-forming regions (Lambrides et al. 2019). This excess seems to be produced by shocks of molecular gas outflows as indicated by the correlation between the H_2 S(3)/PAH 11.3 μm and shock tracers, such as [O I] λ6300/Hα intensity ratio and [O I] λ6300 velocity dispersion (σ; Riffel, Zakamska & Riffel 2020). In Fig. 1, we present a plot of $\sigma_{O I}$ versus the log H_2 S(3)/PAH 11.3 μm ratio, using the data compiled in Riffel, Zakamska & Riffel (2020). NGC 3884 is located at the top-right corner of the plot with a high $\sigma_{O I}$ value, the region where the likely hosts of powerful outflows in molecular gas are expected. Besides NGC 3884, we also identify, in the plot, the galaxy UGC 8782, whose Gemini Multi-Object Spectrograph (GMOS) data were previously presented in Riffel et al. (2023). These two objects, together with the galaxy CGCG 012−070, are the targets of a cycle 1 *JWST* proposal (ID: 1928; PI: R. A. Riffel) aimed to study the warm and hot molecular gas kinematics in these potential hosts of molecular outflows. These galaxies present simultaneously H_2 S(3)/PAH, $\sigma_{O I}$, and [O I] λ6300/Hα in the top 10 per cent highest values observed in the *Spitzer*/SDSS matched sample of Riffel, Zakamska & Riffel (2020). Here, we use optical data to map a hotter counterpart of these outflows, in ionized gas.

In Riffel et al. (2023), we studied the gas kinematics in the inner 3.4×4.9 kpc^2 of UGC 8782 at a spatial resolution of ∼725 pc. We found that the gas kinematics presents two components: (i) a disc component, but which presents deviations from pure rotation, likely due to a previous merger event, and (ii) an outflow, observed as a broad component ($\sigma \gtrsim 200$ km s^{-1}) in all emission lines

blueshifted by ∼150–500 km s^{-1} relative to the systemic velocity of the galaxy in all locations, but with enhanced emission cospatial with a radio hotspot. The kinetic power of the ionized gas outflows corresponds to 1–3 per cent of the AGN bolometric luminosity, above the minimum values required by simulations for AGN feedback to be efficient in suppressing star formation in the host galaxy (Di Matteo, Springel & Hernquist 2005; Hopkins & Elvis 2010; Dubois et al. 2014; Schaye et al. 2015). Here, we present a similar study for the galaxy NGC 3884.

This paper is organized as follows: Section 2 presents the observations and data reduction procedure, while Section 3 presents the results, which are discussed in Section 4. Section 5 summarizes our conclusions. We adopt a distance to NGC 3884 of 115 Mpc based on the Tully–Fisher method (Tully, Courtois & Sorce 2016), for which 1 arcsec corresponds to ∼557 pc at the galaxy.

2 DATA AND MEASUREMENTS

We used the Gemini-North Multi-Object Spectrograph (GMOS; Hook et al. 2004) to observe NGC 3884 using the Integral Field Unit (IFU; Allington-Smith et al. 2002) mode with the B600 grating. The observations were performed on 2021 December 29 under the program code GN-2021B-Q-213 and consisted of five exposures of 1125 s, three of them centred at 650 nm and two at 575 nm, to correct for the detector gaps. We used the GMOS-IFU in the one-slit mode, resulting in a 3.5×5.0 arcsec^2 and covering an observed spectral range of 4450–7300 Å.

The data reduction was performed with the GEMINI.GMOS IRAF package. The procedure includes the subtraction of the bias level, trimming and flat-field correction, background subtraction for each science data, quantum efficiency correction, sky subtraction, and wavelength calibration. We used the LACOS code (van Dokkum 2001) to further remove cosmic rays and finally, we performed the flux calibration, using observations of the standard star HZ 44 to construct the sensitivity function. The final data cube, with an angular sampling of 0.1×0.1 arcsec^2, was constructed by median combining the data cubes for each exposure using the peak of the continuum emission as reference to align them. The velocity resolution is of 89 ± 14 km s^{-1} as measured from the full width at half-maximum (FWHM) of typical emission lines in the CuAr spectra used in the wavelength calibration and the estimated seeing is 0.85 ± 0.13 arcsec as estimated from the FWHM of flux distributions of field stars. This corresponds to a spatial resolution of 475 ± 70 pc at the distance of NGC 3884.

The measurements were performed using the same procedures described in Riffel et al. (2023). In summary, we use the Penalized Pixel-Fitting (PPXF) method (Cappellari & Emsellem 2004; Cappellari 2017, 2023) to fit the contribution of the underlying stellar population on the observed spectra and obtain measurements of the stellar kinematics, using MILES-HC library (Westfall et al. 2019) as spectral templates. Then, we fit the emission-line profiles with two Gaussian curves each, using a continuum-subtracted data cube. We use the IFSCUBE package (Ruschel-Dutra et al. 2021) to fit of the following emission lines: Hβ, [O III] λλ4959, 5007, [O I] λ6300, [N II] λλ6548, 6583, Hα, and [S II] λλ6717, 6731. All emission lines were fitted simultaneously, by adopting the following constraints: (i) the emission line ratios of [O III] λ5007/λ4959 and [N II] λ6548/λ6583 were kept fixed to their theoretical values of 2.98 and 3.06, respectively (Osterbrock & Ferland 2006); and (ii) the centroid velocity and velocity dispersion of emission lines originating from the same species (Hβ and Hα, [O III] λ5007 and [O III] λ4959, [N II] λ6548 and [N II] λ6583, and [S II] λ6717 and
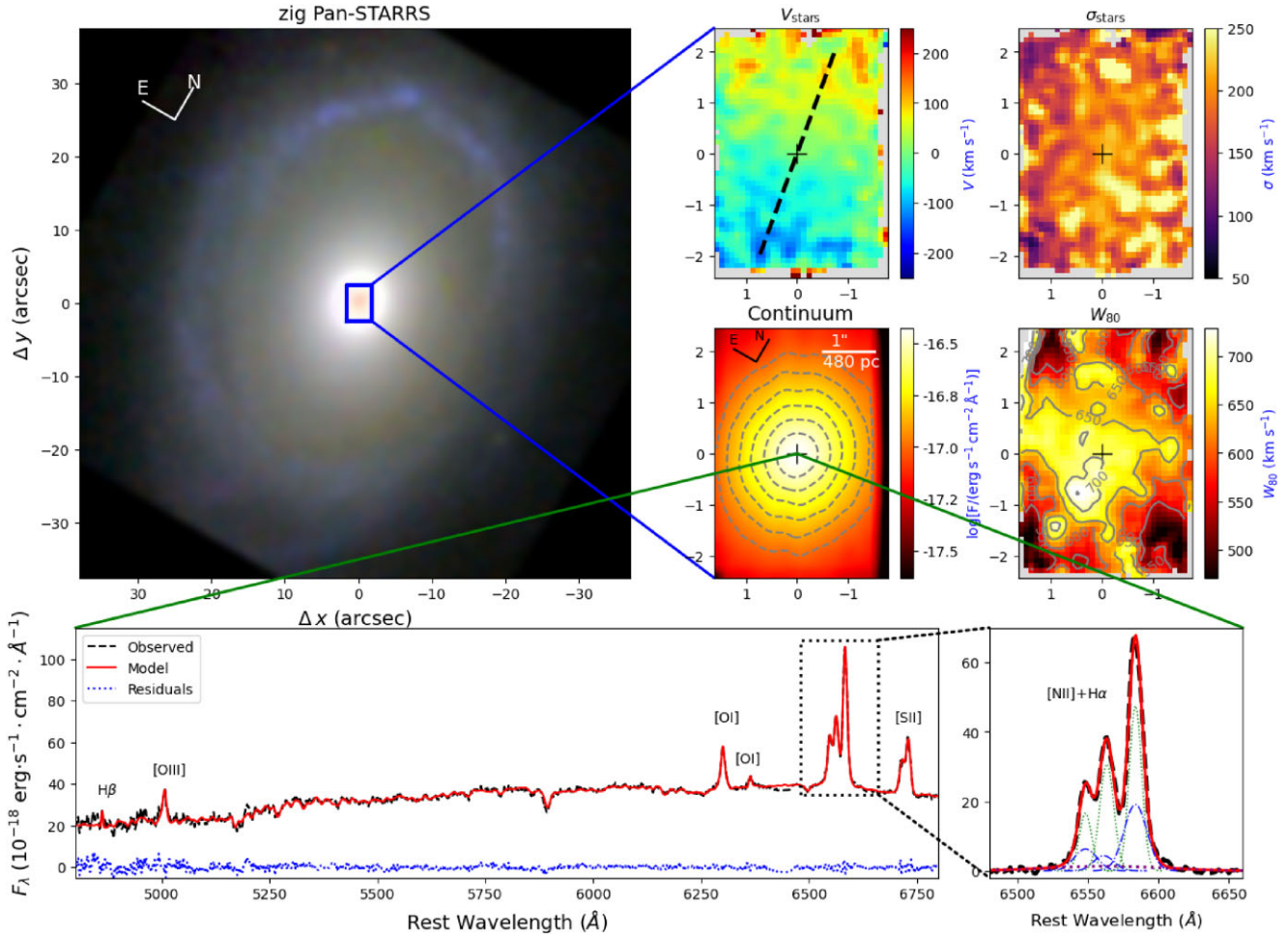
Figure 2. The top-left panel shows a composite image of the 70×70 arcsec^2 in g (4866 Å, shown in blue), i (7545 Å, in green), and y (8679 Å, in red) bands of NGC 3884 using data from the Pan-STARRS archive (Chambers et al. 2016; Flewelling et al. 2020). The top-centre and right panels show the stellar velocity and velocity dispersion maps, respectively. Grey regions in these maps correspond to regions with uncertainties in velocity or σ larger than 50 km s^{-1}. The systemic velocity of the galaxy, defined as the stellar velocity within the inner 0.5 arcsec from the nucleus, has been subtracted from the observed velocity map. The scale bars show the velocities in km s^{-1} and the dashed line represents the orientation of the large-scale disc, as obtained from the r-band SDSS image (Adelman-McCarthy et al. 2008). The central panel shows a GMOS continuum image obtained within a spectral window of 100 Å width centred at 6100 Å. The scale bar shows the continuum flux values in logarithmic units of erg s^{-1} cm^{-2} Å^{-1}. The middle-right panel shows the W_{80} map for the [N II] λ6583 emission line, with the scale bar indicating the values in km s^{-1}. Grey regions represent locations where the line is not detected above three times the standard deviation of the spectra noise. The bottom-left plot shows the observed spectrum for the nuclear spaxel in black, the best-fitting model in red, and the residuals in blue. The strongest emission lines are identified. The bottom-right panel shows a zoom in the [N III] + Hα region to illustrate the multi-Gaussian fit, after subtracting the stellar population contribution. The broad line components are shown in blue and the narrow components are in green. The Hα BLR component is shown as a dotted purple line.

[S II] λ6731) were tied during the fits, for each kinematic component. NGC 3884 is classified as a type 1 AGN and presents a faint Hα emission from the broad-line region (BLR; Véron-Cetty & Véron 2006). No emission associated with the BLR is seen for Hβ. Thus, we include an additional component to reproduce the BLR Hα emission.

Fig. 2 shows a broad overview of the GMOS observations of NGC 3884. The top-left panel shows a large-scale composite image constructed using data from the Panoramic Survey Telescope and Rapid Response System (Pan-STARRS) archive (Chambers et al. 2016; Flewelling et al. 2020), showing in blue the g-band (4866 Å) image, in green the i-band (7545 Å) image, and in red the y-band (8679 Å) image. The spatial orientation is shown in the top-left corner of the image and the inner rectangle shows the GMOS-IFU field of view (FoV). The central panel shows a continuum image

for the central region of NGC 3884 obtained from the GMOS data cube, as the mean fluxes in each spaxel within a spectral window of 100 Å width centred at 6100 Å. This image presents centrally peaked emission, with no dust structures, similarly to the large-scale image. The bottom-left panel shows, as an example, the nuclear spectrum (in black), the best-fitting model (in red), and the residuals of the fit are shown in blue. The model reproduces well the observed spectrum, as indicated by the residuals close to the noise level. The bottom-right panel shows a zoom in the [N II] + Hα region, after subtracting the contribution of the stellar populations. The narrow and broad components are illustrated as green dotted and blue dashed–dotted lines, respectively. The faint very broad Hα component (from the BLR) seen in the nuclear spectrum is shown as a dotted purple line.

3 RESULTS

3.1 Emitting gas structure and kinematics

The top-centre and right panels of Fig. 2 show the stellar velocity field and stellar velocity dispersion map, respectively. The stellar velocity field shows a disc-like rotation pattern with the south side of the disc approaching and the north side receding, with a velocity amplitude of ∼150 km s^{-1} and the line of nodes oriented along the same orientation of the large-scale disc, represented by the black dashed line as derived from the *r*-band SDSS image (Adelman-McCarthy et al. 2008). The stellar velocity dispersion map shows values in the range of 120–230 km s^{-1}. The middle-right panel shows the W_{80} map for the [N II] λ6583 emission line, obtained from the modelled spectra. The [N II] λ6583 emission line was selected because its emission is observed over the whole GMOS-IFU FoV and other emission lines present similar W_{80} maps. This parameter is defined as the width of an emission line comprising 80 per cent of the flux is emitted. It is related to the velocity dispersion (σ) by $W_{80} = 2.563\sigma$ for a Gaussian profile and is commonly used to identify outflows (Zakamska & Greene 2014; Kakkad et al. 2020; Wylezalek et al. 2020; Ruschel-Dutra et al. 2021). W_{80} values larger than 600 km s^{-1} are usually associated with ionized outflows in quasars (e.g. Kakkad et al. 2020), while values above 500 km s^{-1} may already trace AGN winds in lower luminosity AGNs (e.g. Wylezalek et al. 2020). For NGC 3884, the W_{80} map presents values larger than 600 km s^{-1} in most locations, with the highest values reaching 800 km s^{-1} (Fig. 2). These values are higher than those expected from the observed velocity dispersion, using the relation above, and may indicate the presence of outflows in ionized gas.

In Fig. 3, we present the results for the gas emission and kinematics, based on the fitting of the line profiles by Gaussian curves. The first three columns show the flux, centroid velocity, and velocity dispersion maps for the narrow components, respectively. The results for the broad components are shown in the three last columns. From the top to the bottom, we show maps for the [O III] λ5007, [O I] λ6300, Hα, [N II] λ6583, and [S II] λ6731.

The narrow component flux distributions show emission over the whole FoV for the [N II] and Hα, while the most compact distribution is seen for [O I], with extended emission to ∼1.5 arcsec radius from the nucleus. The morphology of the emission-line flux maps is similar to that observed in the Hα narrow-band image obtained with the *Hubble Space Telescope* (Hermosa Muñoz et al. 2022), which shows a rounded structure, with emission peak at the nucleus. The gas velocity fields for all emission lines are similar, showing a rotation pattern with a velocity amplitude of ∼200 km s^{-1}, higher than that seen in the stellar velocity field. In addition, the gas velocity maps show an S-shaped zero velocity structure, not observed for the stars. The gas velocity dispersion maps for the narrow component show values lower than 200 km s^{-1} in most locations, with the highest values seen in the inner 1.0 arcsec radius.

The broad component is detected up to distances of 2 arcsec from the nucleus for the [N II], and a more compact flux distribution is seen for other emission lines. The velocity fields for the [O III] λ5007 and Hα show blueshifts of up to ∼200 km s^{-1}, while the lower ionization lines present values closer to the systemic velocity. The observed velocity dispersion values of the broad component are larger than ∼300 km s^{-1} for all emission lines, with values close to 400 km s^{-1} seen for the [N II] λ6583.

3.2 Emission-line flux ratios

The [O III] λ5007/Hβ, [N II] λ6583/Hα, [O I] λ6300/Hα, and [S II] λλ6717, 6731/Hα flux ratios are frequently used to map the gas excitation in the AGN narrow-line region (NLR) using optical diagnostic diagrams (e.g. Baldwin, Phillips & Terlevich 1981). In comparison to star-forming galaxies, AGN usually presents higher values in the four flux ratios (e.g. Kewley et al. 2001; Kauffmann et al. 2003). Fig. 4 presents the flux ratio maps for the narrow (top panels) and broad (bottom panels) components. We do not show the [O III] λ5007/Hβ map for the broad component, because this component in Hβ is detected only in a few spaxels. For the narrow component, the [O III] λ5007/Hβ shows the highest values of ∼2.5 close to the nucleus and east of it, while the lower ionization lines show the lowest values relative to Hα at the nucleus and the highest values in regions to the east-north-east and west-south-west of the nucleus, approximately along the minor axis of the galaxy. The highest values are ∼2.2, 1.0, and 0.4 for [N II] λ6583/Hα, [S II] λλ6717, 6731/Hα, and [O I] λ6300/Hα, respectively. These values are consistent with typical values observed for AGN (Baldwin, Phillips & Terlevich 1981; Kewley et al. 2001, 2006; Cid Fernandes et al. 2010; Sánchez et al. 2018; Menezes et al. 2022; Ricci et al. 2023). The flux ratio maps for the broad component present overall higher values than those seen in the narrow component, with all regions presenting also typical values observed in AGN.

In Fig. 5, we present the spatially resolved BPT (Baldwin, Phillips & Terlevich 1981) and WHAN (Cid Fernandes et al. 2010, 2011) diagrams for NGC 3884. The BPT diagram for the narrow component reinforces the results above, showing that the flux line ratios for the narrow component are in the range commonly observed for AGNs with almost all spaxels in the region occupied by low-ionization nuclear emission-line regions (LINERs). LINER-like gas emission can also be produced by gas ionization due to hot low-mass evolved stars (HOLMES). The WHAN diagram is useful to separate true AGN emission from retired galaxies, where the gas emission is produced by HOLMES. The WHAN diagram for the narrow component of NGC 3884 shows that some contribution from HOLMES may be present only at distances greater than 1.5 arcsec from the nucleus, while in regions closer to the nucleus the gas emission is associated with the AGN. The WHAN diagram for the broad component shows, nevertheless, values in the region occupied by retired galaxies, with Hα equivalent widths EW$_{H\alpha}$ < 3 Å that can be attributed to HOLMES ionization (Cid Fernandes et al. 2010, 2011; Agostino et al. 2021). However, EW$_{H\alpha}$ as low as 1.5 Å can also be produced by AGN ionization (e.g. Sánchez et al. 2018) and, together with the high values of the [N II] λ6583/Hα, [O I] λ6300/Hα, and [S II] λλ6717, 6731/Hα, indicates that the emission of the broad component is also associated with the nuclear activity.

The Hα/Hβ flux line ratio can be used to investigate the gas extinction. The bottom-left panel of Fig. 4 shows the visual extinction (A_V) for the narrow-line component, calculated from the Hα/Hβ intensity line ratio by (Riffel et al. 2021b)

$$A_V = 7.22 \log \left[\frac{(F_{H\alpha}/F_{H\beta})_{\text{obs}}}{2.86} \right], \tag{1}$$

where $(F_{H\alpha}/F_{H\beta})_{\text{obs}}$ represents the observed Hα/Hβ flux ratio. We adopt the extinction law of Cardelli, Clayton & Mathis (1989) and an intrinsic flux ratio of $F_{H\alpha}/F_{H\beta} = 2.86$ for H I case B recombination in the low-density regime, assuming an electron temperature of $T_e = 10\,000$ K (Osterbrock & Ferland 2006). The observed A_V values for NGC 3884 are in the range 0–4.5 mag.

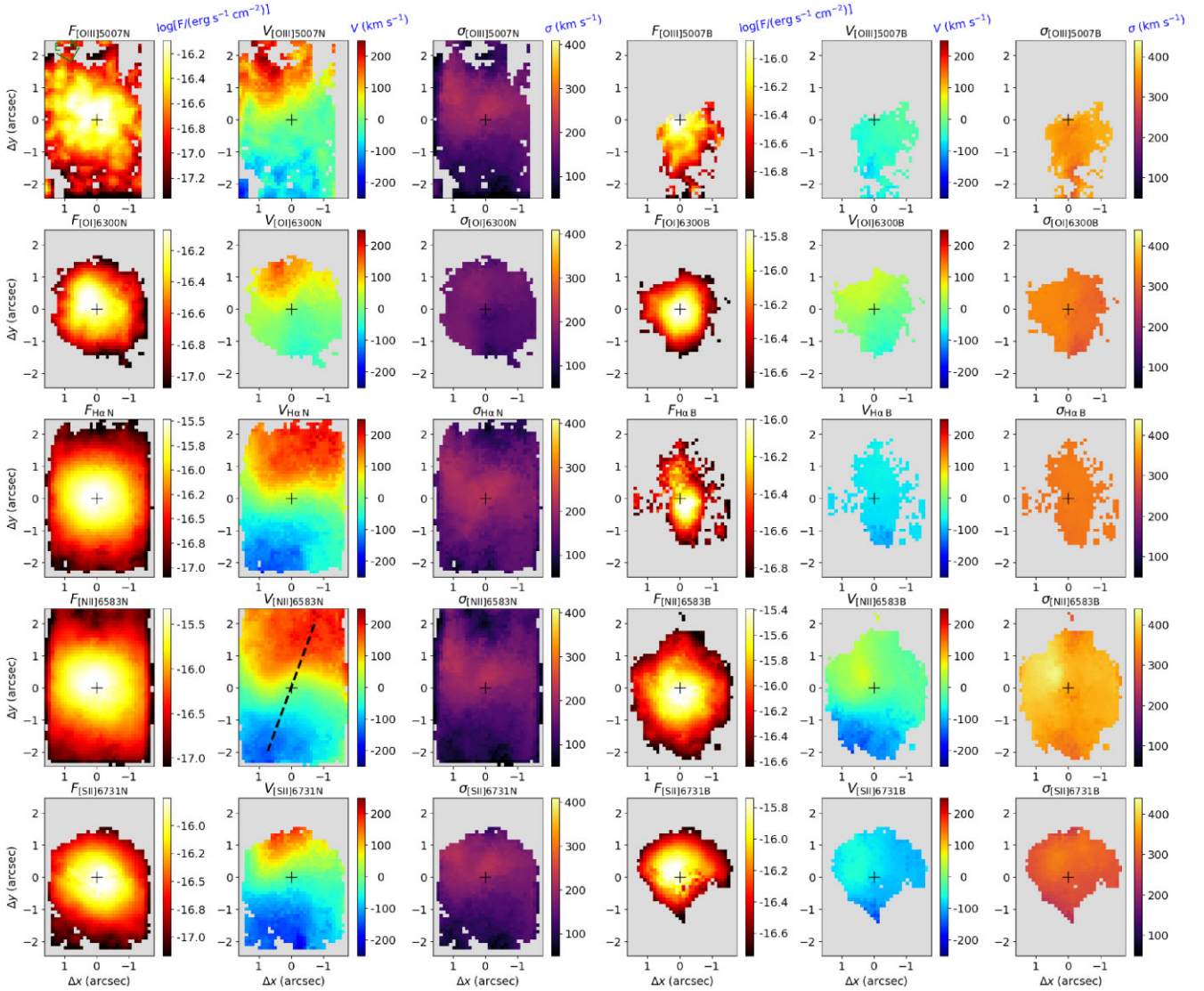**Figure 3.** Gas emission structure and kinematics for NGC 3884. We show the flux distributions and kinematic maps for the [O III] λ5007, [O I] λ6300, Hα, [N II] λ6583, and [S II] λ6731 emission lines, from top to bottom. We display the flux distribution, centroid velocity, and velocity dispersion maps for both the narrow (left three panels) and broad (right three panels) components for each emission line. The scale bars show the line fluxes in logarithmic units of erg s^{-1} cm^{-2} spaxel^{-1}, the velocity and velocity dispersion maps in km s^{-1}, and the continuum image in logarithmic units of erg s^{-1} cm^{-2} Å^{-1} spaxel^{-1}. The location of the continuum peak is identified by the central crosses and the spatial orientation is shown in the top-right panel. The dashed line shows the orientation of the large-scale disc, as obtained from the *r*-band SDSS image (Adelman-McCarthy et al. 2008). Grey regions correspond to locations where the corresponding emission line is not detected above three times the standard deviation of the spectra noise, calculated in the neighbouring spectral regions of each emission line.

Finally, we can map the electron density N_e from the ratio between the fluxes of the [S II] emission lines. We use the PYNEB python package (Luridiana, Morisset & Shaw 2015), assuming an electron temperature of 1.5×10^4 K, a typical value observed in the NLR of nearby AGN (e.g. Revalski et al. 2018, 2021; Dors et al. 2020; Riffel et al. 2021a; Armah et al. 2023). The [S II] doublet can be used to estimate the N_e for flux ratios in the range $0.47 \lesssim F_{\lambda6717}/F_{\lambda6731} \lesssim 1.42$, corresponding to $2.73 \times 10^4 \gtrsim N_e \gtrsim 15$ cm^{-3} (Osterbrock & Ferland 2006). The [S II]-based measurements, in the case of gas being photoionized by an AGN, trace the densities of partially ionized gas zones (Osterbrock & Ferland 2006; Davies et al. 2020). In Fig. 6, the [S II] flux ratio (left) and the resulting N_e (right) maps are shown for the narrow (top) and broad (bottom) components. In the

electron density maps, the yellow regions correspond to high-density clouds, above the limit where the [S II] ratio can be used. The cyan regions represent low-density regions, where $F_{\lambda6717}/F_{\lambda6731} > 1.42$. Both, the narrow and broad component emitting gas show a wide range of N_e values. For the narrow component, the highest densities are observed to the south-west of the nucleus, while the lowest ones are seen to the north-east of it. The opposite behaviour is seen for the broad component, with the highest values observed to the north-east and the lowest ones to the south-west of the nucleus. Using the median values of the observed flux ratios, we estimate densities of ∼7890 and ∼1650 cm^{-3} for the narrow and broad component, respectively.

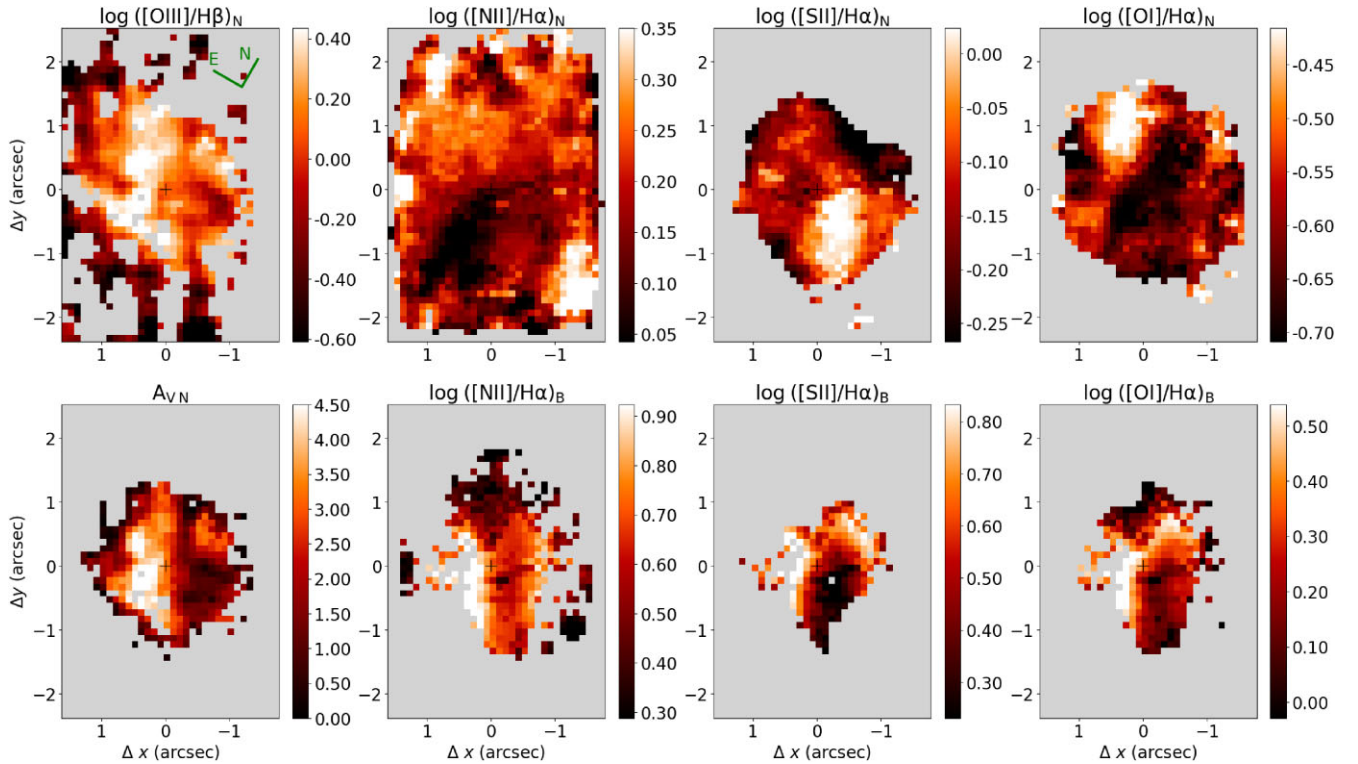**Figure 4.** Emission-line flux ratios for NGC 3884. The top panels show, from left to right, the [O III] λ5007/Hβ, [N II] λ6583/Hα, [S II] λλ6717, 6731/Hα, and [O I] λ6300/Hα ratio maps for the narrow component. The bottom-left panel shows the visual extinction map for the narrow component, derived from the observed Hα/Hβ flux ratios. The remaining three bottom panels show the [N II] λ6583/Hα, [S II] λλ6717, 6731/Hα, and [O I] λ6300/Hα ratio maps for the broad component. In all maps the grey regions correspond to masked locations, where one of both lines are not detected above 3σ of the noise level. The spatial orientation is shown in the top-left panel and the central crosses mark the location of the continuum peak.

4 DISCUSSION

The gas velocity fields for the narrow component (Fig. 3) present a similar rotation pattern to that of the stars (Fig. 2), while the broad component is seen mostly blueshifted relative to the velocity of the stars and presents a larger velocity dispersion. This indicates that the narrow component is produced by gas in the plane of the disc, while the broad component is likely due to a gas outflow, associated with the nuclear activity. From the emission-line ratio maps and diagnostic diagrams, we conclude that the emission of both components is dominated by gas photoionized by the AGN. In this section, we characterize and discuss the kinematics of the disc and the properties of the ionized outflows in the central region of NGC 3884. To the extent of our knowledge, there are no previous spatially resolved observations of the gas and stellar kinematics of NGC 3884 in the literature.

4.1 The disc component

The stellar velocity field (Fig. 2) and the gas velocity fields for the narrow components of the emission lines (Fig. 3) present a well-defined rotation pattern. We use the KINEMETRY method (Krajnovic et al. 2006) to model the stellar and gas velocity field from the [N II] λ6583 narrow component. The spatially resolved velocity fields are modelled by KINEMETRY in elliptical rings centred at the galaxy's nucleus, by finding the best-fitting parameters of a harmonic expansion of the velocity distribution within each ring.

In Fig. 7, we present the KINEMETRY results for NGC 3884. The top panels show, from left to right, the observed stellar velocity field,

the KINEMETRY model, and a residual map, obtained by subtracting the model from the observed velocities. The middle panels show the results for the [N II] λ6583 emission line, with the maps in the same order as those for the stars. For both, gas and stars, the resulting models reproduce well the observed velocities, as evidenced by the low residual values, which are smaller than 20 km s^{-1} at most locations.

The bottom panels of Fig. 7 show, from left to right, the radial variation of the major axis kinematic position angle (PA) of the fitted ellipses and the harmonic coefficients k_1 and k_5/k_1, respectively. The red stars are based on the modelling of the stellar velocity field, while the blue ones are for the [N II] kinematics. The k_1 parameter characterizes the velocity amplitude of bulk gas motions, while the k_5/k_1 ratio measures deviations beyond pure rotation in higher orders (Krajnovic et al. 2006).

As can be seen in the bottom-left panel of Fig. 7, the kinematic PAs of the stars are in agreement with the photometric PAs obtained by modelling the GMOS continuum image using the PHOTUTILS package (Bradley et al. 2020). Some discrepancy is seen in for distances smaller than 0.6 arcsec and beyond 1.8 arcsec, where the fits of the kinematic PA is less constrained due to the small number of points. In the inner ~1.2 arcsec, the gas kinematic PAs are displaced from the stellar kinematic PAs by up to ~60°, in agreement with the distortions seen in the gas velocity field. Such misaligned gas and stellar discs are usually interpreted as being due to externally acquired gas in previous merger events (e.g. Davis et al. 2011; Raimundo et al. 2017; Li et al. 2021; Raimundo 2021; Raimundo, Malkan & Vestergaard 2023). Another possible explanation for the observed gas kinematics is that the distortion is produced by streaming motions of gas towards the
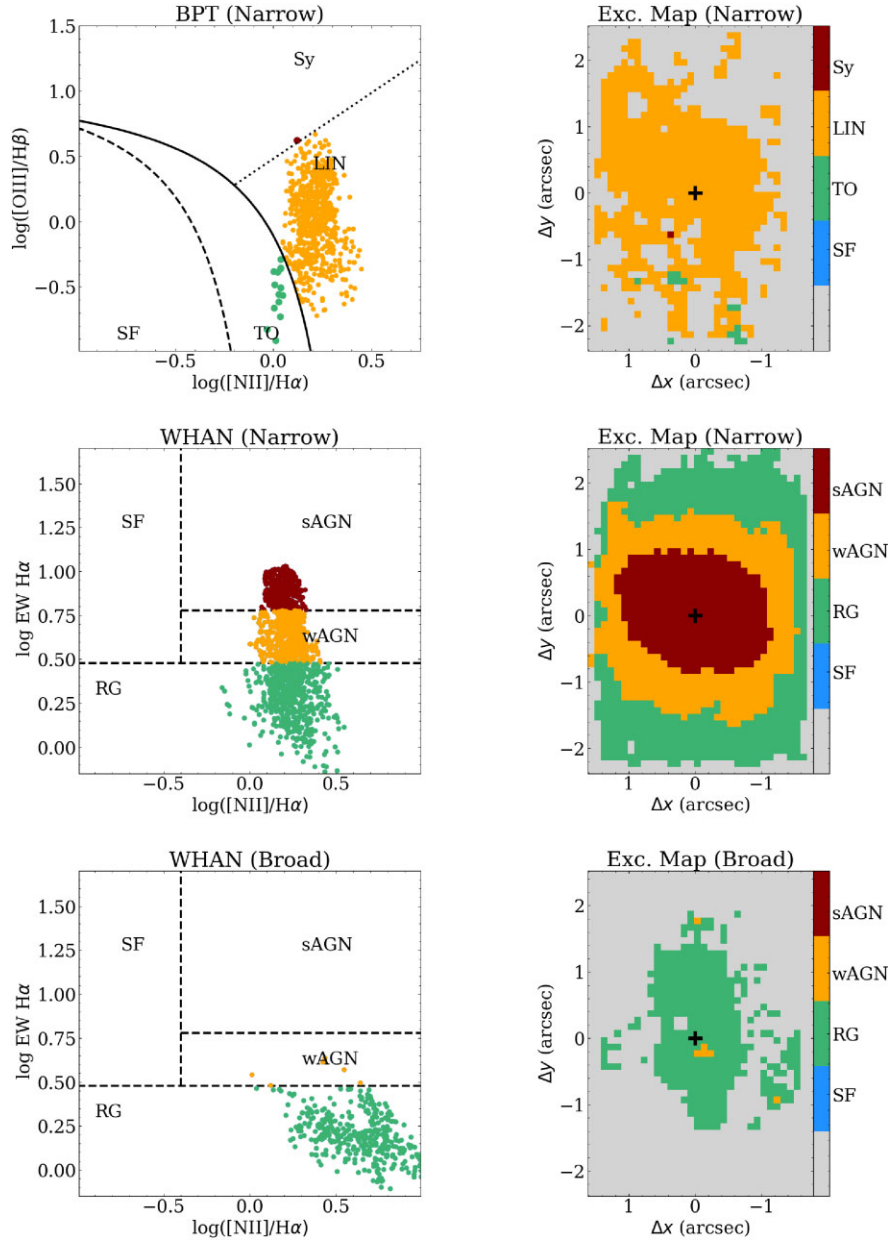
Figure 5. BPT (Baldwin, Phillips & Terlevich 1981) and WHAN (Cid Fernandes et al. 2010, 2011) diagrams for NGC 3884. The top panels show the BPT diagram (left) and the colour-coded excitation map (right) for the narrow component. The boundary lines from Kewley et al. (2001), Kauffmann et al. (2003), and Cid Fernandes et al. (2010) are represented by continuous, dashed, and dotted lines, respectively. We do not display the BPT diagram for the broad component due to the non-detection of the [O III] and Hβ lines in most spaxels. The middle and bottom panels illustrate the WHAN diagrams and the corresponding excitation maps for the narrow and broad components, respectively. The lines in the WHAN diagram follow the definitions provided by Cid Fernandes et al. (2011), separating star-forming galaxies (SF), transition objects (TO), weak AGN (wAGN; i.e. LINERs), strong AGN (sAGN; i.e. Seyferts), and retired galaxies (RG). In the excitation maps, the grey regions represent locations where at least one line is not detected above the 3σ limit.

centre, superimposed to the rotation disc component. Such inflows of gas along the disc are seen in redshifts at the near side of the galaxy and in blueshifts at its far side and has been commonly reported in nearby low-luminosity AGN (e.g. Storchi-Bergmann et al. 2007; Schnorr-Müller et al. 2014; Brum et al. 2017; Storchi-Bergmann & Schnorr-Müller 2019; Bianchin et al. 2022). The extinction map (Fig. 4) shows the highest values to the east, indicating this is the near side of the galaxy disc, consistent with the location where a redshifted distortion is observed in the gas velocity field (Fig. 3).

Finally, the distortions seen in the gas velocity field could also be produced by the interaction of the outflow with the gas in the disc.

The bottom-centre panel of Fig. 7 shows that the gas velocity amplitude is larger than that of the stars at all radii. This difference may be due to projection effects due to distinct distributions of the gas and stars in the galaxy, as the gas is expected to be located in a thin disc, while the stars present a larger velocity dispersion due the contribution of bulge stars. Finally, the low values of k_5/k_1 (bottom-right panel of Fig. 7) indicate that there is no significant
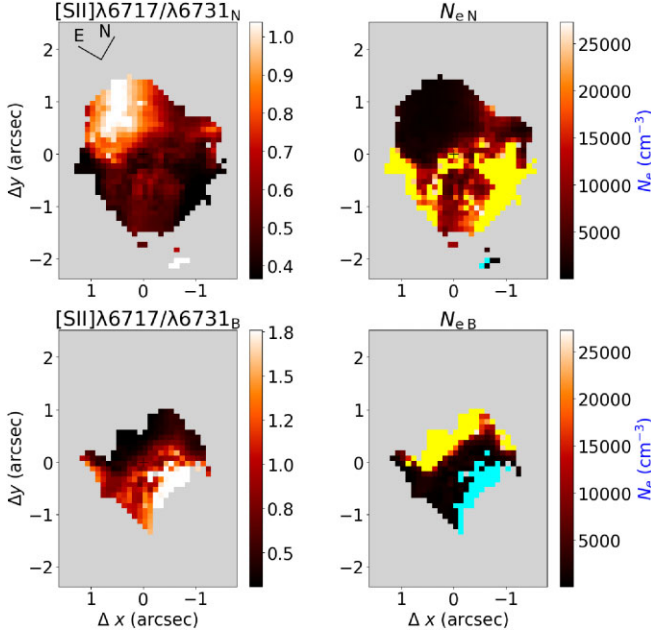
Figure 6. $F_{\lambda6717}/F_{\lambda6731}$ flux ratio (left) and [S II]-based electron density (right) maps for the narrow (top) and broad (bottom) components. The grey regions correspond to locations where one or both emission lines are not detected above the 3σ noise level. The yellow regions represent high-density clouds, where the [S II] lines are not sensitive to the density with $F_{\lambda6717}/F_{\lambda6731} < 0.47$. The cyan locations correspond to low-density regions with $F_{\lambda6717}/F_{\lambda6731} > 0.42$. The central cross marks the position of the continuum emission peak and the spatial orientation is shown in the top-left panel.

deviation from pure rotation, for both stars and gas producing the narrow component in the emission lines.

4.2 Ionized gas outflows

As mentioned above, we interpret the blueshifted-broad component in the emission lines as being due to outflows in ionized gas. This interpretation is in agreement with previous results based on long-slit observations of NGC 3884, which report the presence of a similar broad component, originated from nuclear outflows (Cazzoli et al. 2018; Hermosa Muñoz et al. 2022). We follow the procedure used in Riffel et al. (2023) and estimate the mass outflow rate and kinetic power of outflows within circular rings with width $\Delta R = 0.3$ arcsec, centred at the nucleus using

$$\dot{M}_{\mathrm{out},\Delta R} = \sum_i \frac{M^i_{\mathrm{out},\Delta R} V^i_{\mathrm{out},\Delta R}}{\Delta R} \qquad (2)$$

and

$$\dot{K}_{\mathrm{out},\Delta R} = \sum_i \frac{M^i_{\mathrm{out},\Delta R} (V^i_{\mathrm{out},\Delta R})^3}{2\Delta R}, \qquad (3)$$

where $M^i_{\mathrm{out},\Delta R}$ corresponds to the mass of ionized gas within the ring at velocity channel i, and $V^i_{\mathrm{out},\Delta R}$ represents the outflow velocity modulus. The sum is performed over velocity bins of $\sim$45 km s^{-1}, corresponding to the spectral sampling of the data, within the range from -1500 to 1500 km s^{-1} relative to the systemic velocity of the galaxy. We generated velocity channel maps for the Hα outflow component from a data cube obtained after subtracting the contribution of the stellar population, the narrow and Hα BLR components, and

the [N II] narrow and broad components. We compute the mass of the outflow within each channel by

$$M_{\mathrm{ion}} \approx 7 \times \frac{L_{\mathrm{H}\alpha}}{N_{\mathrm{e}}}, \qquad (4)$$

using the Hα luminosity of the broad component within each bin, corrected by extinction ($L_{\mathrm{H}\alpha}$) using the extinction law from Cardelli, Clayton & Mathis (1989) and a visual extinction of $A_V = 0.5$ mag computed using equation (1) and the Hα and Hβ fluxes of the broad component measured using an integrated spectrum within a circular aperture of 0.5 arcsec radius centred at the position of the continuum peak. We adopt $N_{\mathrm{e}} = 1650$ cm^{-3}, the medium value for the broad component, as estimated from the [S II] doublet.

Fig. 8 shows the resulting radial profiles of the mass outflow rate (top panel) and the kinetic power of the ionized gas outflows (bottom panel) in NGC 3884. The error bars represent the propagated uncertainties from the flux measurements. The maximum values of the mass outflow rate and kinetic power of the outflows are, respectively, 0.25 ± 0.15 M$_\odot$ yr^{-1} and $(8.4 \pm 1.8) \times 10^{40}$ erg s^{-1} and are observed at 1.2 arcsec (670 pc) from the nucleus. The kinetic power of the outflow corresponds to $\sim$0.06 per cent of the AGN bolometric luminosity, estimated by $L_{\mathrm{bol}} = 3500 L_{\mathrm{[O III]}}$ (Heckman et al. 2004), where $L_{\mathrm{[O III]}} \approx 2.1 \times 10^{41}$ erg s^{-1} is the extinction-corrected [O III] $\lambda5007$ luminosity measured within a circular aperture of 0.5 arcsec centred at the nucleus.

The minimum powers of outflows required by theoretical prediction to AGN feedback become effective in suppressing star formation in the host galaxy are in the range 0.05–$2L_{\mathrm{bol}}$ (Di Matteo, Springel & Hernquist 2005; Hopkins & Elvis 2010; Dubois et al. 2014; Schaye et al. 2015; Weinberger et al. 2017). In Fig. 9, we present a plot of the kinetic power of ionized outflows versus the AGN bolometric luminosity using the data presented in Riffel et al. (2021c), including measurements for more than 600 objects spanning seven orders of magnitude in AGN luminosities. The blue filled region is obtained by computing the mean values of the outflow kinetic power plus and minus its standard deviation, within bins of 0.5 dex in bolometric luminosity. The observed kinetic coupling efficiency ($\dot{E}_{\mathrm{K}}/L_{\mathrm{bol}}$) for ionized outflows in NGC 3884 is similar to those observed in AGNs of similar luminosities and below the minimum values predicted by simulations, as can be seen in Fig. 9. We have also included the results for UGC 8782 obtained by Riffel et al. (2023). The maximum values of the mass outflow rate and kinetic power of the ionized outflows for UGC 8782 are 0.5 ± 0.1 M$_\odot$ yr^{-1} and $(6.8 \pm 1.1) \times 10^{41}$ erg s^{-1}, respectively. As pointed out in Riffel et al. (2023), the outflows observed in UGC 8782 are mechanically driven by the interaction of the radio jet with the ambient gas, while in NGC 3884 the outflows are likely driven by the AGN radiation field, as it does not present strong radio emission. In addition, as extensively discussed in the literature (e.g. Harrison et al. 2018; Richings & Faucher-Giguère 2018), it is improbable that all the injected energy by the AGN is converted into kinetic power in the outflow. Therefore, a cautious approach is needed when directly comparing the observed kinetic power of the outflows with model predictions. In addition, AGN winds are seen in multigas phase phenomena and other gas phases (e.g. molecular) should be taken into account.

For low-luminosity AGNs, such as in the case of NGC 3884, winds produced by a hot accretion flow around the SMBH can be effective in quenching star formation in the galaxy if the winds are sustained for more than $\sim$1 Myr (Almeida, Nemmen & Riffel 2023). The mass of the SMBH of NGC 3884 is $\sim$1.5 $\times 10^8$ M$_\odot$ as obtained from the M–σ relation (McConnell et al. 2011) using the median value of the
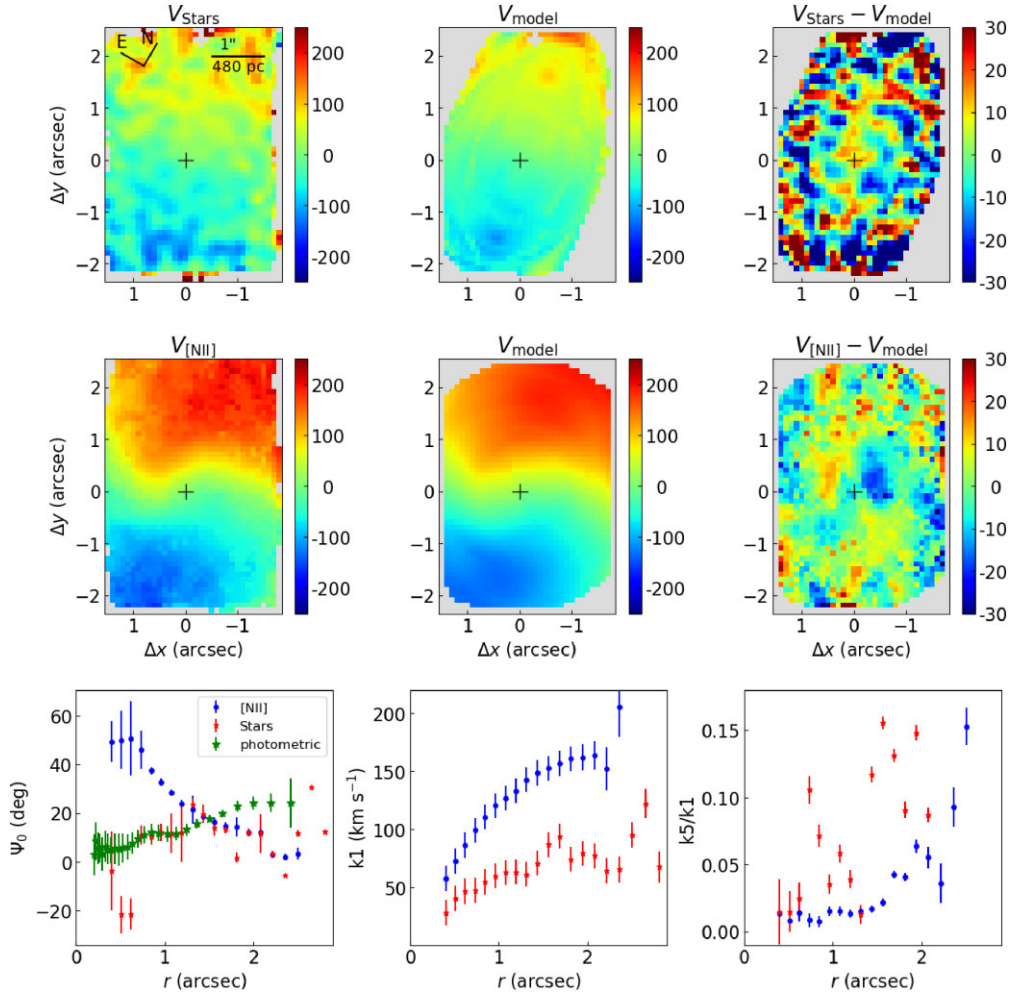
Figure 7. KINEMETRY results for NGC 3884. Top panels: Observed stellar velocity field, best-fitting model using the KINEMETRY code and residual velocity map (observed minus model). Middle panels: Same as the top panels, but for the [N II] λ6583 emission line. Bottom panels: The left panel displays a plot of the position angle (PA) of the major axes of the modelled ellipses as function of radius. The red stars represent the kinematic PAs of the stars, while the blue circles represent the kinematic PAs of the [N II] emitting gas. The photometric PA obtained by fitting the continuum image using the PHOTUTILS package is shown as green stars. The central and right panels illustrate the harmonic expansion coefficients k_1 and k_5/k_1 obtained from the KINEMETRY model.

stellar velocity dispersion of $\sigma \approx 190$ km s^{-1}. Using this mass value, together with the kinetic power of the ionized outflow in NGC 3884 and the predictions of the wind model of Almeida, Nemmen & Riffel (2023), we find that the observed winds are powerful enough to quench at least 10 per cent of the star formation in the host galaxy.

5 CONCLUSIONS

We used optical IFS of the inner 1.9×2.8 kpc^2 of the low-luminosity AGN host NGC 3884 to map the stellar and gas emission structure and their kinematics. Our main conclusions are listed below.

(i) The stellar kinematics is dominated by a rotation disc component with the kinematic PA ranging from $\sim 0°$ at the smallest radii to $\sim 20°$ beyond ~ 1 kpc, consistent with the photometric PA obtained from the continuum image.

(ii) Extended gas emission is detected over most of the GMOS FoV, and emission-line ratio diagnostic diagrams indicate that the emission is produced by AGN ionization. An unresolved Hα nuclear component associated with the AGN BLR is detected.

(iii) The gas kinematics presents two components, as evidenced by the detection of narrow and a broad component in the line profiles. The narrow component is due to gas emission in the disc, while the broad component is associated with AGN-driven outflows.

(iv) The gas disc component presents a kinematic PA similar to that of the stars for distances larger than 1.2 arcsec (670 pc) from the nucleus, while a difference of up to $\sim 60°$ is seen at smaller radii.

(v) The deviations of the narrow component from the disc kinematics can be attributed to gas inflows along nuclear spirals (redshifts in the far and blueshifts in the near side of the galaxy plane), which seem to be common in early-type AGN; alternatively, it could be due to interaction of the broad-component outflow with the ambient gas.

(vi) We estimate a maximum mass outflow rate of 0.25 ± 0.15 M$_\odot$ yr^{-1} and a maximum kinetic power of $(8.4 \pm 1.8) \times 10^{40}$ erg s^{-1}. The kinetic power corresponds to ~ 0.06 per cent of the AGN bolometric luminosity.

(vii) By comparing the wind kinetic power with theoretical predictions of winds produced by a hot accretion flow in low-luminosity AGN, we conclude that the observed winds are powerful enough to quench more than 10 per cent of the star formation in the host galaxy.
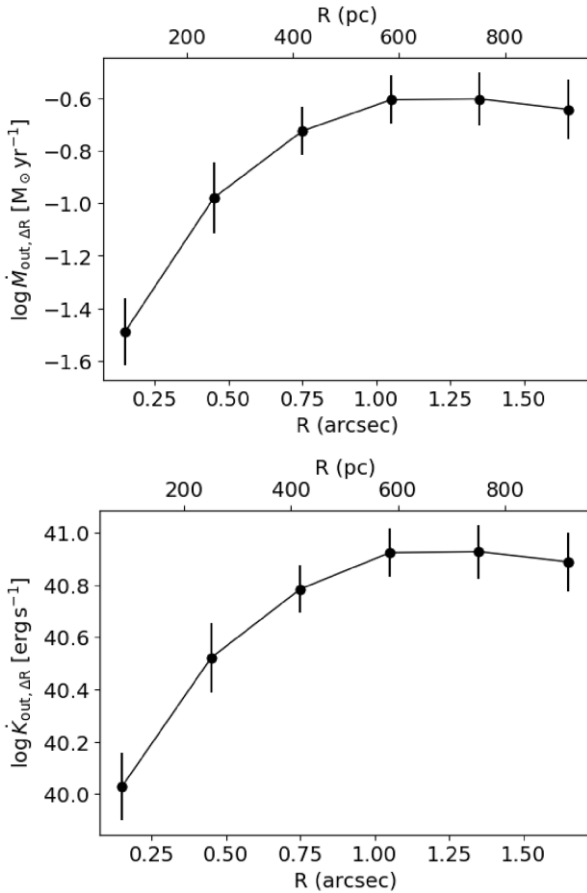
This galaxy thus seems to show both inflows and outflows in ionized gas. Our next step will be to analyse the kinematics of the molecular gas that should be more abundant than the ionized gas (e.g. Veilleux et al. 2020) and reveal the most important process for SMBH versus galaxy co-evolution: feeding or feedback?

Figure 8. The top panel displays the radial profile of the mass outflow rate, while the bottom panel illustrates the radial profile of the kinetic power of the ionized outflows in NGC3884.
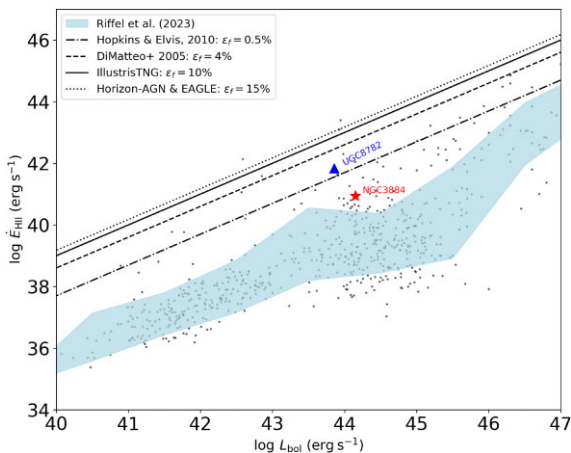
Figure 9. Plot of the kinetic power of the outflows versus the AGN bolometric luminosity using the data presented in Riffel et al. (2021c), represented by the black small circles. The light blue region shows the mean values of the kinetic power of ionized outflows plus and minus the 1σ deviation, computed within bins of 0.5 dex in bolometric luminosity. The lines show the minimum outflows coupling efficiencies necessary to be effective in suppressing star formation, predicted by different simulations (Di Matteo, Springel & Hernquist 2005; Hopkins & Elvis 2010; Dubois et al. 2014; Harrison et al. 2018; Xu et al. 2022). UGC 8782 is represented by the blue triangle, using the values derived by Riffel et al. (2023). The position of NGC 3884 is indicated as a black star.

DATA AVAILABILITY

The processed data used in this paper will be shared on reasonable request to the corresponding author.

REFERENCES

Adelman-McCarthy J. K. et al., 2008, ApJS, 175, 297
Agostino C. J. et al., 2021, ApJ, 922, 156
Allington-Smith J. et al., 2002, PASP, 114, 892
Almeida I., Nemmen R., Riffel R. A., 2023, MNRAS, 526, 217

Armah M. et al., 2023, MNRAS, 520, 1687

Baldwin J. A., Phillips M. M., Terlevich R., 1981, PASP, 93, 5

Bianchin M. et al., 2022, MNRAS, 510, 639

Binney J., Tabor G., 1995, MNRAS, 276, 663

Blanton M. R. et al., 2017, AJ, 154, 28

Bradley L. et al., 2020, astropy/photutils: 1.0.0 (1.0.0). Zenodo. Available at: https://doi.org/10.5281/zenodo.4044744

Brum C., Riffel R. A., Storchi-Bergmann T., Robinson A., Schnorr Müller A., Lena D., 2017, MNRAS, 469, 3405

Caglar T. et al., 2020, A&A, 634, A114

Cappellari M., 2017, MNRAS, 466, 798

Cappellari M., 2023, MNRAS, 526, 3273

Cappellari M., Emsellem E., 2004, PASP, 116, 138

Cardelli J. A., Clayton G. C., Mathis J. S., 1989, ApJ, 345, 245

Cazzoli S. et al., 2018, MNRAS, 480, 1106

Chambers K. C. et al., 2016, preprint (arXiv:1612.05560)

Cicone C. et al., 2014, A&A, 562, A21

Cid Fernandes R., Stasińska G., Schlickmann M. S., Mateus A., Vale Asari N., Schoenell W., Sodré L., 2010, MNRAS, 403, 1036

Cid Fernandes R., Stasińska G., Mateus A., Vale Asari N., 2011, MNRAS, 413, 1687

Comerón S., Knapen J. H., Ramos Almeida C., Watkins A. E., 2021, A&A, 645, A130

Costa T., Rosdahl J., Sijacki D., Haehnelt M. G., 2018, MNRAS, 479, 2079

Couto G. S., Storchi-Bergmann T., Siemiginowska A., Riffel R. A., Morganti R., 2020, MNRAS, 497, 5103

Dall'Agnol de Oliveira B. et al., 2021, MNRAS, 504, 3890

Dall'Agnol de Oliveira B., Storchi-Bergmann T., Morganti R., Riffel R. A., Ramakrishnan V., 2023, MNRAS, 522, 3753

Davies R. et al., 2020, MNRAS, 498, 4150

Davis T. A. et al., 2011, MNRAS, 417, 882

Di Matteo T., Springel V., Hernquist L., 2005, Nature, 433, 604

Dors O. L., Maiolino R., Cardaci M. V., Hägele G. F., Krabbe A. C., Pérez-Montero E., Armah M., 2020, MNRAS, 496, 3209

Dubois Y. et al., 2014, MNRAS, 444, 1453

Elvis M., 2000, ApJ, 545, 63

Ferrarese L., Merritt D., 2000, ApJ, 539, L9

Feruglio C., Maiolino R., Piconcelli E., Menci N., Aussel H., Lamastra A., Fiore F., 2010, A&A, 518, L155

Feruglio C. et al., 2015, A&A, 583, A99

Flewelling H. A. et al., 2020, ApJS, 251, 7

Frank J., King A., Raine D. J., 2002, Accretion Power in Astrophysics, 3rd edn. Cambridge Univ. Press, Cambridge

Gebhardt K. et al., 2000, ApJ, 539, L13

Graham A. W., Sahu N., 2023, MNRAS, 518, 2177

Gunn J. E. et al., 2006, AJ, 131, 2332

Harrison C. M., Costa T., Tadhunter C. N., Flütsch A., Kakkad D., Perna M., Vietri G., 2018, Nat. Astron., 2, 198

Heckler K. F., Ricci T. V., Riffel R. A., 2022, MNRAS, 517, 5959

Heckman T. M., Kauffmann G., Brinchmann J., Charlot S., Tremonti C., White S. D. M., 2004, ApJ, 613, 109

Hermosa Muñoz L., Márquez I., Cazzoli S., Masegosa J., Agís-González B., 2022, A&A, 660, A133

Hook I. M., Jørgensen I., Allington-Smith J. R., Davies R. L., Metcalfe N., Murowinski R. G., Crampton D., 2004, PASP, 116, 425

Hopkins P. F., Elvis M., 2010, MNRAS, 401, 7

Juneau S. et al., 2022, ApJ, 925, 203

Kakkad D. et al., 2020, A&A, 642, A147

Kakkad D. et al., 2022, MNRAS, 511, 2105

Kauffmann G. et al., 2003, MNRAS, 346, 1055

Kewley L. J., Dopita M. A., Sutherland R. S., Heisler C. A., Trevena J., 2001, ApJ, 556, 121

Kewley L. J., Groves B., Kauffmann G., Heckman T., 2006, MNRAS, 372, 961

King A., 2003, ApJ, 596, L27

Krajnovic D., Cappellari M., De Zeeuw P. T., Copin Y., 2006, MNRAS, 366, 787

Lambrides E. L., Petric A. O., Tchernyshyov K., Zakamska N. L., Watts D. J., 2019, MNRAS, 487, 1823

Li S.-l. et al., 2021, MNRAS, 501, 14

Liu G., Zakamska N. L., Greene J. E., Nesvadba N. P. H., Liu X., 2013, MNRAS, 436, 2576

Luridiana V., Morisset C., Shaw R. A., 2015, A&A, 573, A42

McConnell N. J., Ma C.-P., Gebhardt K., Wright S. A., Murphy J. D., Lauer T. R., Graham J. R., Richstone D. O., 2011, Nature, 480, 215

Magorrian J. et al., 1998, AJ, 115, 2285

Menezes R. B., Steiner J. E., Ricci T. V., da Silva P., 2022, MNRAS, 513, 5935

Osterbrock D. E., Ferland G. J., 2006, Astrophysics of Gaseous Nebulae and Active Galactic Nuclei, 2nd edn. University Science Books, Mill Valley, CA

Peng C. Y., 2007, ApJ, 671, 1098

Raimundo S. I., 2021, A&A, 650, A34

Raimundo S. I., Davies R. I., Canning R. E. A., Celotti A., Fabian A. C., Gandhi P., 2017, MNRAS, 464, 4227

Raimundo S. I., Malkan M., Vestergaard M., 2023, Nat. Astron., 7, 463

Ramos Almeida C., Piqueras López J., Villar-Martín M., Bessiere P. S., 2017, MNRAS, 470, 964

Revalski M., Crenshaw D. M., Kraemer S. B., Fischer T. C., Schmitt H. R., Machuca C., 2018, ApJ, 856, 46

Revalski M. et al., 2021, ApJ, 910, 139

Ricci T. V., Steiner J. E., Menezes R. B., Slodkowski Clerici K., da Silva M. D., 2023, MNRAS, 522, 2207

Richings A. J., Faucher-Giguère C.-A., 2018, MNRAS, 478, 3100

Riffel R. A., Zakamska N. L., Riffel R., 2020, MNRAS, 491, 1518

Riffel R. A. et al., 2021a, MNRAS, 501, L54

Riffel R. et al., 2021b, MNRAS, 501, 4064

Riffel R. A. et al., 2021c, MNRAS, 504, 3265

Riffel R. A., Riffel R., Bianchin M., Storchi-Bergmann T., Souza-Oliveira G. L., Zakamska N. L., 2023, MNRAS, 521, 3260

Rupke D. S. N. et al., 2019, Nature, 574, 643

Ruschel-Dutra D. et al., 2021, MNRAS, 507, 74

Sánchez S. F. et al., 2018, Rev. Mex. Astron. Astrofis., 54, 217

Schaye J. et al., 2015, MNRAS, 446, 521

Schnorr-Müller A., Storchi-Bergmann T., Nagar N. M., Ferrari F., 2014, MNRAS, 438, 3322

Shimizu T. T. et al., 2019, MNRAS, 490, 5860

Silk J., 2017, ApJ, 839, L13

Silk J., Rees M. J., 1998, A&A, 331, L1

Storchi-Bergmann T., Schnorr-Müller A., 2019, Nat. Astron., 3, 48

Storchi-Bergmann T., Dors O. L., Jr, Riffel R. A., Fathi K., Axon D. J., Robinson A., Marconi A., Östlin G., 2007, ApJ, 670, 959

Tully R. B., Courtois H. M., Sorce J. G., 2016, AJ, 152, 50

van Dokkum P. G., 2001, PASP, 113, 1420

Veilleux S., Maiolino R., Bolatto A. D., Aalto S., 2020, A&AR, 28, 2

Véron-Cetty M. P., Véron P., 2006, A&A, 455, 773

Weinberger R. et al., 2017, MNRAS, 465, 3291

Westfall K. B. et al., 2019, AJ, 158, 231

Wylezalek D., Flores A. M., Zakamska N. L., Greene J. E., Riffel R. A., 2020, MNRAS, 492, 4680

Xu Y., Luo Y., Kang X., Li Z., Li Z., Wang P., Libeskind N., 2022, ApJ, 928, 100

Zakamska N. L., Greene J. E., 2014, MNRAS, 442, 784

This paper has been typeset from a TEX/LATEX file prepared by the author.